

Lattice dynamics and Raman spectrum of supertetragonal PbVO₃.

P. Bouvier^{1*}, A. Sasani², E. Bousquet², M. Guennou³, J. Agostinho Moreira⁴

¹ *Université Grenoble Alpes, Institut Néel CNRS, 25 Rue des Martyrs, 38042, Grenoble, France.*

* pierre.bouvier@neel.cnrs.fr

² *Université de Liège, CESAM, QMAT, Physique Théorique des Matériaux, 19 Allée du 6 aout, B-4000, Sart Tilman, Belgium.*

³ *Department of Physics and Materials Science, University of Luxembourg, 41 rue du Brill, L-4422 Belvaux, Luxembourg.*

⁴ *IFIMUP – Instituto de Física de Materiais Avançados, Nanotecnologia e Fotónica, Departamento de Física e Astronomia, Faculdade de Ciências da Universidade do Porto. Rua do Campo Alegre s/n. 4169-007 Porto, Portugal.*

Abstract:

Lead vanadate PbVO₃, with a polar *P4mm* symmetry, is isostructural with the model soft-mode driven ferroelectric PbTiO₃, but differs from it by the so-called “supertetragonal” elongation of its unit cell. In this paper, we report a combined study of the lattice dynamics of PbVO₃ by Raman spectroscopy at room temperature and first-principle calculations. All zone-center transverse optical (TO) phonon modes are identified by polarized, angle-dependent Raman spectroscopy and assigned as follows: E modes at 136, 269, 374 and 508 cm⁻¹, A₁ modes at 188, 429 and 874 cm⁻¹ and the B₁ mode at 320 cm⁻¹. The calculations confirm the experimental symmetry assignment. Besides, we analyze the mode eigenvectors in detail, in order to identify the atomic displacements associated with each mode and compare them with PbTiO₃. In spite of their differences in chemistry and strain, the phonon eigenvectors are found to be remarkably comparable in both compounds. We discuss the position of the ferroelectric soft mode in PbVO₃ as compared to PbTiO₃. A sizeable splitting of the B₁+E modes appears as a characteristic feature of supertetragonal phases. The peculiarity of the vanadyl V-O bond frequency in PbVO₃ is also addressed.

Keywords: lead vanadate, supertetragonal perovskite, polarized Raman spectroscopy, DFT simulations, lattice dynamics

1. Introduction

Non-centrosymmetric tetragonal perovskites have been attracting the attention of the scientific community because they exhibit high electric polarization and piezoelectric coefficients which make them promising materials for functional devices. The model ferroelectric PbTiO₃, which crystallizes in the *P4mm* space group at room conditions, combines polar distortions from cation off-centering displacements and stereochemical effect of the Pb²⁺ 6s² lone pair electrons, attaining an electric polarization of 57(3) to 70 μC.cm⁻² respectively measured or calculated [1,2]. From phenomenological model, it is expected that the electric polarization is coupled to the tetragonal strain [2], thus highly elongated unit cells will display larger polarization. This has attracted attention on the family of so-called “supertetragonal” polar perovskites that include PbVO₃, BiFeO₃ films under compressive strain [3], BiCoO₃ [4], Bi₂ZnVO₆ [5], solid solutions between them [6,7] or even BiMnO₃ between 40 and 55 GPa [8]. They are characterized by an elongation ratio *c/a* around 1.2, way larger than in classical ferroelectric perovskites where it reaches at most 1.08. Besides, many of these compounds are also magnetic, which makes them potentially attractive multiferroics.

PbVO₃ can be synthesized at high-temperature and high-pressure, and recovered at room conditions in the tetragonal structure of *P4mm* space group with $a = 3.80005(6) \text{ \AA}$, $c = 4.6703(1) \text{ \AA}$ and $c/a \approx 1.23$ [9,10]. The PbVO₃ structure is perovskite based. However, due to the large tetragonal deformation and the presence of a short V-O vanadyl bond length, the three-dimensional octahedral network is rather considered as layers of corner-shared VO₅ pyramids [9,10]. The polar structure is stable from 12 to 570 K, above which it oxidizes in Chervetite Pb₂V₂O₇ [9,10]. Under increasing hydrostatic pressure, it is stable until 2.5 GPa, which corresponds to a $c/a = 1.14$, before collapsing onto a cubic *Pm-3m* perovskite structure via a first-order transition, with a volume drop of 10 % [10,11]. The exceptionally large tetragonality and the atomic positions obtained from synchrotron x-ray powder diffraction data suggest that the ferroelectric polarization should reach $150 \mu\text{C}/\text{cm}^2$ from Berry-phase calculations [12]. The non-centrosymmetric, polar, piezoelectric and likely ferroelectric structure was ascertained from second-harmonic generation measurements in the 4 to 400 K temperature range [13]. To the best of our knowledge, ferroelectric switching has not yet been demonstrated in PbVO₃, but past experience has shown that switching of supertetragonal ferroelectric was possible in BiFeO₃ films [14] and we anticipate that PbVO₃ could be switched as well in suitable conditions.

With its V⁴⁺ cation in a $3d^1$ configuration, PbVO₃ is expected to be magnetic. First-principle calculations have predicted that PbVO₃ should display a two-dimensional antiferromagnetism (of C-type or G-type) ground state, as a result of the ordering of the d_{xy} electronic orbitals [12,15,16]. However, there is still no consensus about its magnetic structure. The antiferromagnetic transition was first claimed from the observation of a maximum at 180 K in the temperature dependent magnetization curve, although, according to muon spin rotation experiments, the long-range ordering is not established above 43 K [16]. Magnetic susceptibility and specific heat measurements have suggested that PbVO₃ exhibits a magnetic frustration and should rather be considered as a disordered $\frac{1}{2}$ spin square lattice [17]. No sign of ferromagnetic ordering could be observed [18] nor calculated using first-principles [19] under high-pressure.

Lattice dynamics of PbVO₃ has been scarcely studied and little is known about its Raman signature. According to Singh's calculations, three fully symmetric modes are predicted at 190 cm^{-1} , 408 cm^{-1} and 838 cm^{-1} in the *P4mm* structure; the later high wavenumber mode being assigned to the short and stiff V-O vanadyl bond vibration [15]. Unpolarized Raman spectra of PbVO₃ powder, synthesized at high-temperature and high-pressure, were published by Okos *et al.* [20]. They observed at least eight modes at 187, 210, 263, 316, 370, 506, 876 and 942 cm^{-1} and have proposed a mode and symmetry assignments. The Raman spectra of PbVO₃ thin films deposited on (001)-oriented LaAlO₃ substrates, displays two broad bands at 830 cm^{-1} and 930 cm^{-1} , which were assigned to the TO-LO components of the short V-O symmetrical stretching mode, and an intense band at 593 cm^{-1} assigned to the long V-O stretching mode [21]. Additional low wavenumber peaks were reported at 390, 350, 220 and 190 cm^{-1} and assigned to V-O-V bending modes and vibrations involving heavy Pb cations [21]. Similarly, broad bands with weak intensity were reported on other PbVO₃ thin films [22]. Besides, those measurements show the presence of a double peak at 965 cm^{-1} which is usually associated with other vanadate species (VO_x). Overall, the lack of a comprehensive assignment of the Raman-active phonons in PbVO₃ hinders the use of Raman spectroscopy for investigations of the physics of PbVO₃.

In this paper, we address this problem by a combination of angle-resolved polarized spectroscopy study of the Raman intensity on a single crystal at room temperature, complemented with first-principles lattice dynamics calculations. We show how this approach allows us to successfully identify all phonon modes and their symmetries. Besides, we address the relevance of the comparison

between lattice dynamics of PbTiO_3 and PbVO_3 by a detailed analysis of the mode eigenvectors calculated by first-principle.

2. Methodological details

PbVO_3 samples were synthesized by Okos *et al.* [20] using solid-state reaction method at high-temperature and high-pressure. The absence of any parasitic phase was attested from the previously recorded X-ray powder diffraction [20]. The average crystals sizes are smaller than 15 μm .

The Raman spectra were recorded at room conditions in the backscattering geometry, using the final stage of a T64000 Jobin-Yvon spectrometer equipped with 1800 /mm grating blazed at 500 nm. The 514.5 nm and 488 nm lines of an Ar^+ laser (Spectra Physics Stabilite2017) were chosen for excitation. Semrock® Maxline and Razor edge were used to clean and reject the stray laser line before entering the spectrometer. The laser was focused on the sample surface with an x50 objective (Olympus NA=0.75), which allows a 2 μm diameter laser spot on the sample. During our preliminary studies, we observed that the tetragonal phase may transform into Chervetite ($\text{Pb}_2\text{V}_2\text{O}_7$) under intense laser irradiation. The later exhibits a totally different Raman spectrum, easily recognized by an intense band centered at 900 cm^{-1} (see Figure S.1 in Supplemental Information). The decomposition of PbVO_3 in Chervetite is expected at a temperature higher than 570 K [9,10]. We found that reducing the incident laser power on the sample as low as 0.4 mW (as measured after the objective), using a broadband neutral density filter, avoids sample degradation.

The crystal was centered in a specific holder allowing to rotate the sample by 360° around the vertical axis, coincident with the incident and scattered light directions, ensuring that measurements are performed at the exact same position on the sample surface during the entire 360° rotation.

For the polarized Raman measurements, we consider two reference frames sharing the common vertical y -axis, as shown in Figure 1. The first reference frame (x,y,z) is fixed on the sample and has the x - and z -axes parallel to the a and c crystallographic axes, respectively, the latter being coincident with the optical axis of the tetragonal crystal. The laboratory reference frame (X,Y,Z) has the V- and H-polarization directions in the horizontal plane parallel to the X - and Z - axes, respectively. As the crystallographic orientation of the sample was initially unknown, the angle between Z - and z -axes is defined as θ_o . This value is found *a posteriori* from the quantitative analysis of the angular dependence of the Raman intensity measured under chosen fixed polarizations of the incident laser and of the analyzed scattered signal, while the sample is rotated over an azimuthal angle θ from 0° to 180°. We measured all three $y(\text{VV})y$, $y(\text{HV})y$ and $y(\text{VH})y$ configurations, in the Porto notation. A sum of independent damped oscillators was fitted to the Raman spectra, using IgorPro® software, to extract the angular dependence of the wavenumber, the half width at half maximum and the intensity of each individual band.

Our first-principles density functional theory (DFT) study of PbVO_3 was done using the CRYSTAL17 software package [23]. We have used the HSE06 hybrid functional for the exchange correlation term [24,25]. The structural and phonon frequencies were found to be converged by using a 8x8x8 k-points mesh sampling and the structure were relaxed until the forces are less than $3 \cdot 10^{-5}$ Ha/Bohr. The phonon calculations were done using the frozen phonon technique as implemented in Crystal17 [26,27]. We have used the Gaussian type basis sets from reference [28], [29] and [30] for Pb, V and O, respectively, which give the best structural agreement with experiment. The truncation thresholds in the evaluation of the Coulomb and exchange series present in the CRYSTAL code were adjusted to 10^{-7} for Coulomb overlap tolerance, 10^{-7} for Coulomb penetration tolerance, 10^{-7} for exchange overlap

tolerance, 10^{-7} for exchange pseudo-overlap in the direct space, and 10^{-14} for exchange pseudo-overlap in the reciprocal space. The symmetry of the different structures and the phonon modes were determined using the FINDSYM software [31]. The calculation of the energy of the different magnetic phases shows that the C-type antiferromagnetic ordering is the ground state in agreement with previous DFT calculations [9,12,15,16,17], such that all the calculations reported below were performed in this magnetic phase.

3. Results and discussion

3.1. Group theory prediction of Raman modes symmetry

Factor group analysis of the PbVO_3 structure ($4mm$, C_{4v} point group) yields the following decomposition of the optical normal modes in eight irreducible representations at the Γ -point of the Brillouin zone:

$$\Gamma^{opt} = 3A_1 + B_1 + 4E \quad (1)$$

The Wyckoff positions occupied by the different atoms in the primitive cell and their contributions to the Raman-active modes are given in Table 1.

The A_1 and E modes are simultaneously infrared and Raman-active, while the B_1 mode is only Raman-active. It is also useful to recall that the A_1 and E modes originate from the three optical modes of the T_{1u} irreducible representation in the O_h point group of the parent cubic perovskite (space group $Pm\bar{3}m$, $Z=1$), whereas the B_1 and the fourth E modes originate from the T_{2u} irreducible representation [32,33]. Because the A_1 and E modes are infrared-active, the transverse (TO) and longitudinal (LO) optical modes are splitted according to the Lyddane-Sachs-Teller relation [34,35].

3.2. Raman spectra of PbVO_3 at room conditions and sample orientation

Representative Raman spectra of PbVO_3 recorded in the HV-scattering geometry using the 514.5 nm and the 488 nm laser lines as excitation, are shown in Figure 2. Both spectra display eight well-defined bands which matches the expectations from the group theory analysis. It is worth stressing that the low wavenumber band at 136 cm^{-1} is sometimes hidden by the scattered signal arising from rotational modes of O_2/N_2 molecules present in the air. The observed very low intensity broad bands between 750 and 900 cm^{-1} are associated to small traces of spurious phase, likely associated with Chervetite formed during the synthesis process. The observation of only the eight expected Raman active modes and no hints of the TO-LO splitting is due to the fact that the optical axis of the crystal (parallel to the c -axis) is in the plane perpendicular to the incoming laser propagation direction (\vec{k}_i) (see Figure 1). In this case, only the TO modes are probed.

3.3. Angular dependence of the Raman intensity and symmetry assignment.

Representative Raman spectra recorded in the $100 - 1000 \text{ cm}^{-1}$ spectral range, using the 514.5 nm line as excitation, in the (a) VV- and (b) HV-scattering geometries for several selected azimuthal angles, are presented in Figure 3. The intensity of the Raman bands depends on both the scattering geometry and the orientation of the incident electric field relatively to the a - and c - crystallographic axes, defined by the azimuthal angle $\theta + \theta_o$ (see Figure 1). The angular dependence of the Raman intensity is given by the following equation:

$$I(\theta) \propto |\hat{e}_i \mathcal{R}(\theta) \cdot T \cdot \mathcal{R}^{-1}(\theta) \hat{e}_s|^2 \quad (2)$$

where \hat{e}_i and \hat{e}_s are the unit vectors of the incident and scattered electric field, respectively, and $\mathcal{R}(\theta)$ is the rotation matrix referred to the laboratory reference frame. T is the Raman tensor written in the crystal principal axes.

Assuming the experimental geometry shown in Figure 1, the rotation matrix about the Y-axis is:

$$\mathcal{R}(\theta) = \begin{pmatrix} \cos(\theta + \theta_o) & 0 & \sin(\theta + \theta_o) \\ 0 & 1 & 0 \\ -\sin(\theta + \theta_o) & 0 & \cos(\theta + \theta_o) \end{pmatrix} \quad (3)$$

where θ_o accounts for the initial angle between the z-axis (// to c-axis) and the Z-axis (// to H-axis) (see Figure 1).

The Raman tensors T in the $4mm$ (C_{4v}) point group can be written as follows:

$$A_1 = \begin{pmatrix} \alpha & 0 & 0 \\ 0 & \alpha & 0 \\ 0 & 0 & \beta \end{pmatrix} \quad (4)$$

$$B_1 = \begin{pmatrix} \gamma & 0 & 0 \\ 0 & -\gamma & 0 \\ 0 & 0 & 0 \end{pmatrix} \quad (5)$$

$$E = \begin{pmatrix} 0 & 0 & \delta \\ 0 & 0 & \delta \\ \delta & \delta & 0 \end{pmatrix} \quad (6)$$

where α, β, γ and δ are considered as real tensor elements. Using equations (2) to (6), the azimuthal angular dependence of the intensity of the Raman bands associated with the different symmetry modes can be calculated for each scattering geometries, which are given in Table 2.

According to Equations (7) to (15), the A_1 , B_1 and E modes can be clearly distinguished from the angular dependence of the spectral intensity in both the VV and HH configurations. For instance, each of the A_1 and the B_1 modes displays twofold symmetric lobes, whereas the E modes display fourfold symmetric lobes. The A_1 and B_1 modes can also be distinguished as their lobes are rotated by 90° relatively to each other. The E modes are distinguished from the A_1 and B_1 modes as their lobes are rotated by 45° from the A_1 or B_1 modes. In cross-polarization geometry, HV (or VH), the intensity of both A_1 and B_1 modes exhibits the same fourfold symmetric lobes, so they cannot be distinguished. These considerations will allow to assign a symmetry to the observed Raman bands of PbVO_3 , based on their intensity variations recorded with azimuthal angle at all scattering geometries.

3.3.1. E-modes

Figure 4 shows the polar plot of the angular dependence of the intensity of the Raman bands centered at 136, 269, 374 and 508 cm^{-1} , measured in the VV- and VH-scattering geometries, respectively. In all geometries, the $I(\theta)$ exhibits fourfold symmetric lobes, whose orientation is rotated by 45° in the cross-polarization (VH in fig. 4; HV not shown). The solid lines were determined by the best fit of equations (13-14) to the experimental results, respectively. The excellent agreement between experiment and theory allows us to unequivocally assign these modes to the E symmetry. The same initial position $\theta_o = 33(1)^\circ$ is determined for all the four E modes in all considered geometries. The δ values of the Raman tensor, extracted for the four E modes, are reported in Table 3. These values are dependent on the scattering geometries of the experimental setup (VV, VH or HV). No attempt was done to correct for this instrument response. Instead all values are reported in Table 3.

3.3.2. A_1 modes

Figure 5 shows the polar plot of the angular dependence of the intensity of the Raman bands at 188, 429 and 874 cm^{-1} , measured in the VV and VH-scattering geometries, respectively. In the VV-scattering geometry, the intensity of the bands at 188 and 874 cm^{-1} displays two prominent broad lobes, whereas for the band at 429 cm^{-1} it exhibits a fourfold lobe structure. The orientation of the four lobes is rotated 45° relatively to the lobes observed for the E modes, which excludes the possibility that this band has E symmetry. We notice that the width and shape of the lobes for the A_1 modes are strongly dependent on the values taken by α and β tensor coefficients. If these values are close to each other, the twofold lobe will become a circle, showing a $I(\theta)$ independent on the azimuthal angle. However, if $\alpha \approx -\beta$, we expect a fourfold symmetric lobe. This is exactly what we observed for the three modes, allowing us to assign these bands to A_1 modes. The solid lines in Figure 5 were determined by the best fit of equations (7-8) to the experimental results, respectively. The same initial angle $\theta_o = 35(3)^\circ$ is found for all the three A_1 modes in all considered geometries. The α and β element values of each A_1 Raman tensor are reported in Table 3. The anisotropic tensor ratio between the Raman tensor elements is $\beta/\alpha=1.19(2)$ for the 188 cm^{-1} mode whereas, the ratio is $\beta/\alpha=1.81(5)$ for the 874 cm^{-1} mode, and $\beta/\alpha=-0.91(4)$ for the 429 cm^{-1} band, with one tensor element taking a negative value. Interestingly, the anisotropy of the Raman tensor at 874 cm^{-1} is much larger than for the two other modes. In the cross-polarization VH (or HV) geometries, the fourfold lobe of the 188 and 874 cm^{-1} modes are not perfectly reproduced by equation (8) that should produce four symmetric lobes, which are likely due to some depolarisation of the Raman signal.

3.3.3. B_1 mode

Figure 6 shows representative best fit of the Raman spectra of PbVO_3 in the 220-350 cm^{-1} spectral range, recorded in a scattering geometry and at an azimuthal angle where the intensity of the band at 320 cm^{-1} is maximum. The band at 319 cm^{-1} has an asymmetric shape resembling the Fano-type interference [36]. The polar plot of the angular dependence of the intensity of this Raman band, measured in the VV and VH-scattering geometries, is presented in Figure 7. The largest amplitude lobes in the VV-geometries are perfectly described by equation (10) and are oriented along a direction that is rotated 90° relatively to the A_1 modes, as it is expected for B_1 modes. The same initial angle of $\theta_o = 34(2)^\circ$ is found from the position of the maximum intensity of the lobes. The γ values of the Raman tensor are reported in Table 3. We notice that in the crossed polarisation, the fourfold lobes are not perfectly reproduced by the equation (11) that should yield four symmetric lobes. These small imperfections are likely due to some depolarisation of the Raman signal, which as for A_1 modes, is very sensitive for this mode. Despite this discrepancy, we have assigned a B_1 symmetry to this mode.

3.4. Lattice dynamical calculations for PbVO_3 and comparison with experiment

Table 4 summarizes the experimental wavenumber values of the observed TO Raman-active modes and the corresponding symmetry assignment, and compares with the ones obtained from our first-principle calculations. The agreement between experimental and calculated results is very good. The schematic representations of the atomic displacements involved in each phonon mode obtained from our DFT simulations are presented in Figure 8 along with the calculated wavenumbers. The eigendisplacements are reported in Table S.2 in Supplemental Information. The largest wavenumber deviation between experiment and simulation is found for the highest A_1 mode at 907 cm^{-1} , with more than 30 cm^{-1} upshift with respect to the experiment. This A_1 mode only involves the vanadyl bond V-O(1) stretching, with a bond length $d_{\text{V-O}}=1.668(8)$ Å as reported from original X-ray diffraction

measurement on PbVO_3 [9,10]. According to the Badger's rule $\nu^{2/3} \propto d^{-1}$ [37], the stretching frequency ν of chemical bonds is an inverse function of the bond length d involved in the vibration. Thus the comparison with other vanadyl containing compounds such as CaV_2O_5 ($\omega = 932 \text{ cm}^{-1}$; $d_{\text{V-O}} = 1.645 \text{ \AA}$) [38], $\alpha'\text{-NaV}_2\text{O}_5$ ($\omega = 972 \text{ cm}^{-1}$; $d_{\text{V-O}} = 1.60 \text{ \AA}$) [39], $\alpha\text{-V}_2\text{O}_5$ ($\omega = 997 \text{ cm}^{-1}$; $d_{\text{V-O}} = 1.585 \text{ \AA}$) [40,41,42] (see Figure S.3 in Supplemental Information) shows that the V-O bond in PbVO_3 is not only longer but also its strength is weaker, compared to other vanadate compounds. In the early calculations by Singh [15], this mode was found at an even lower position of 838 cm^{-1} (see Table 4). The next highest deviation is found for the E mode at 349 cm^{-1} with a difference of 26 cm^{-1} with the experimental position. Other modes show better agreement with deviations of less than 5 cm^{-1} .

The discrepancies between the experimental and predicted wavenumber values here reported, can originate from different factors: (i) the exchange correlation functional used here or (ii) the fact that the calculations were done at 0 K within the C-type antiferromagnetic phase while the Raman experiment was done at room temperature in the paramagnetic phase. In order to estimate the importance of magnetic order as a source of discrepancy between theory and experiment, we have also calculated the phonon frequencies in the ferromagnetic (FM), AFM C-type, AFM G-type and AFM-A type phases of PbVO_3 . This revealed a rather strong spin-phonon coupling for some modes. For example, the E modes at 349 cm^{-1} and at 269 cm^{-1} can be shifted by up to 30 cm^{-1} between the FM, AFM C-type and AFM G-type. This strong spin-phonon coupling may contribute to explain the discrepancy between theory and experiment but does not modify the mode assignment nor the following discussion of the eigenvectors.

3.5 Comparison between phonon modes in PbVO_3 and PbTiO_3 .

PbTiO_3 and PbVO_3 are isostructural and have both the cubic perovskite as a parent high-symmetry structure; it is therefore tempting to make links between their Raman modes. However, it is also natural to expect that the major differences in chemical bonding and strain result in significant mode mixing that make a one-to-one mapping hazardous. In order to explore the relevance of this comparison, we analyzed in more details the phonons of PbVO_3 and PbTiO_3 . Specifically, in order to analyze the effect of the c/a ratio, we made the following computational experiment. We computed an artificial PbTiO_3 cell, named PTO-ST, whereby the volume and the c/a ratio were fixed to the experimental values of PbVO_3 and the internal atomic coordinates relaxed. Doing so, we obtained relaxed atomic positions (Table S.4 in Supplemental Information), born effective charges (Table S.5 in Supplemental Information), and hence polarization very similar to those of PbVO_3 ($117 \mu\text{C}/\text{cm}^2$ in PbTiO_3 vs $132 \mu\text{C}/\text{cm}^2$ in PbVO_3). In other words, PbTiO_3 strained artificially to a super-tetragonal cell adopts a microscopic structure very close to that of PbVO_3 .

We then computed the phonon frequencies in this artificial "supertetragonal" phase of PbTiO_3 , which we report in Table 5. To highlight how the phonons of PTO-ST compare with those of PbVO_3 , we report the overlap (i.e. projections of mode eigenvectors) between PbTiO_3 and PbVO_3 eigenvectors (also reported in Table 5). We observe that all the PbTiO_3 eigenvectors have an almost perfect correspondence with those of PbVO_3 with overlap values above 0.87 in all cases. Most phonon frequencies show moderate differences (up to 40 cm^{-1}), with two remarkable exceptions. First, the high frequency A_1 mode shows a large discrepancy of 138 cm^{-1} . Second, the characters of the intermediate E(2) and E(3) modes are swapped, the overlaps shows a small mode mixing, and the frequency of the E(3) modes differ by 72 cm^{-1} . Even so, it is legitimate to consider that the overlap between phonon eigenvectors is very good and to establish a one-to-one correspondence between the modes in PbTiO_3 and PbVO_3 . Overall, this indicates that the difference in chemistry between

PbTiO₃ and PbVO₃ does not affect too much the phonon eigenvectors if they are calculated at the same cell parameters.

The correspondence between the Raman signatures of PbVO₃ and PbTiO₃ is presented schematically in Figure 9. We report in black and red colors the two specific polarization configurations that highlight either the E or A₁ modes in both single crystals. The Raman spectrum of PbTiO₃ reported on the top is measured on a reference single crystal. The vertical bars and the dotted lines between them sketch, respectively, for the band position and the correspondence between Raman modes of each E, A₁ or B₁ symmetries as the c/a ratio increases from c/a=1.06 in PbTiO₃ to c/a=1.25 in PbVO₃.

Notice that the B₁ mode at 320 cm⁻¹ in PbVO₃ has an asymmetric line shape, nicely fitted with a Fano-type line profile. This asymmetric shape was also reported for the A₁ TO phonon in polar *P4mm* BaTiO₃ at 170 cm⁻¹ [43], or in PbTiO₃ at 147 cm⁻¹ [44,45] or for the TO₂ phonon in the non-polar *I4/mcm* SrTiO₃ at low temperature [46] and have been subject of discussions to understand their origin. In PbVO₃, the peak shape is not dependent on the laser excitation wavelength which rules out any resonant electron-phonon origin for this asymmetry. Here we observe that the asymmetrical shape is located at higher energy in the supertetragonal PbVO₃ compared to other regular polar *P4mm* perovskites. The interference between two acoustical phonons state (2TA) and a transversal optic phonon located at the same energy has been proposed to explain the unusual peak shape [43].

A remarkable feature of the phonon spectrum of PbVO₃ as compared with PbTiO₃ is the sizeable splitting between the modes B₁ and E stemming from the silent T_{2u} mode from the cubic phase. This splitting is in principle allowed in uniaxial crystals but is generally only observed for the A₁ and E modes [33], while the spectral separation between B₁ and E mode is usually so small that it cannot be resolved [47]. Here, we have measured a 51 cm⁻¹ splitting between the B₁ and E modes at 319 cm⁻¹ and 269 cm⁻¹ respectively, in good agreement with the 56 cm⁻¹ calculated by DFT. Even larger B₁+E spectral separation of 208 cm⁻¹ were calculated from DFT simulations in BiCoO₃ compound [48] that display a larger tetragonal strain, c/a=1.267(1) [4], compared to PbVO₃. A sizeable splitting of the E and B₁ mode therefore appears as a characteristic feature associated to supertetragonal phases.

The comparison between Raman signature of PbVO₃ and PbTiO₃ shows that all phonons wavenumbers are higher in PbVO₃ as compared to PbTiO₃, in spite of the fact that the volume is larger. For the two lowest wavenumber A₁ and E modes, if we compare the position in wavenumber of those two modes in PbTiO₃ and in PbVO₃, we notice that while the unit cell volume increase, the wavenumber increases from 88 to 138 cm⁻¹ for E mode and from 147 to 188 cm⁻¹ for A₁ mode. The low wavenumber A₁ and E modes involve antisymmetric displacements either along the c-axis or in the x/y plane of the Pb atoms against the rigid VO₅ in PbVO₃. These modes can be considered as sensitive to the strength of the lead-oxygen bonds and the fact that we observe a shift toward higher wavenumbers as the volume increases indicates that the lead-oxygen force constant is increasing from PbTiO₃ to PbVO₃. Thus, our Raman measurements show some hardening of the Pb-O bond in PbVO₃. This result agrees with recent first principle calculations of electron density in the PbTi_{1-x}V_xO₃ solid solutions that have shown that the vanadium substitution enhances the covalent interaction of the Pb-O bonds [49] which is expected to increase its bond strength.

3.6 Comparison with the modes of the cubic perovskite: tracking the ferroelectric soft mode

PbTiO₃ serves as a model for soft-mode driven ferroelectrics. As such, its soft optic mode and its lattice dynamics have been the subject of many works over decades in order to understand their details and their relation to the dielectric properties [50,51,52,53]. As it is well known, when calculated by first

principles, cubic PbTiO_3 has one unstable T_{1u} mode whose eigenvector also corresponds to the atomic displacements required to take cubic PbTiO_3 to the tetragonal phase [54]. This makes it a classical “soft-mode”. It is however only one of the three T_{1u} modes allowed so that hybridization with other T_{1u} modes is in principle possible, either under the effect of temperature and anharmonicity, or by chemical substitution. The phase transition in PbVO_3 , on the other hand, is very different in character: it occurs under pressure at 2.5 GPa as a strongly first-order transition with a very large volume drop of 10 % [11]. It cannot be called soft-mode driven in a spectroscopic sense, but the concept can be used nonetheless based on the phonon eigenvectors.

In our calculations with the HSE06 functional and the CRYSTAL code, we could not access to the simulation of phonons in the cubic phase of PbVO_3 due to the closure of the band gap and the disappearance of the magnetic order, so that we cannot compare the cubic phonons of PbVO_3 with those of its supertetragonal phase. However, as the phonon eigenvectors of supertetragonal PbTiO_3 are similar to those of PbVO_3 , we can see how the phonon eigenvectors of ground state PbVO_3 project onto those of cubic PbTiO_3 . We have calculated the phonons of the cubic phase of PbTiO_3 and in Table 6 we show the projections of the PbVO_3 ground state phonon eigenvectors against those of cubic PbTiO_3 . The eigendisplacements are reported in Table S.6 in Supplemental Information.

The overlaps of the mode eigenvectors are best discussed by separating the modes according to their symmetries. We leave here aside the B_1 mode which is not polar and also constrained by symmetry to overlap perfectly with the T_{2u} silent mode of the cubic phase. Considering first the overlap of the soft mode with the A_1 modes in the ground state of PbTiO_3 , we observe and confirm that the soft mode does not correspond to the lowest A_1 mode but spread over all three of them, with a dominant contribution on the intermediate $A_1(2)$ at 367 cm^{-1} . The same is true when considering the PbVO_3 , with an even larger overlap with the highest $A_1(3)$ mode at 909 cm^{-1} . The lowest $A_1(1)$ mode of PbTiO_3 overlaps dominantly with the first stable polar mode of the cubic phase, and this trend is even more pronounced in supertetragonal PbVO_3 .

The analysis of the E modes leads to similar conclusions, albeit with some additional complexity. First of all, the E mode from T_{2u} clearly has to be considered since it becomes polar at the phase transition and mixes with the neighboring E mode, as described previously. As a consequence, when considering the overlaps in Table 6, one should bear in mind the swapping of the E(2) and E(3) modes characters described in the previous section. With these precautions however, it is clear that the trend observed the A_1 modes is also reflected in the E mode eigenvectors. It therefore appears that there is a continuity in the lattice dynamics of PbTiO_3 and PbVO_3 , whereby the soft phonon mode keeps shifting upwards, gradually transferring its character to modes of higher frequencies, while the displacements of the two other polar modes, in contrast, are shifted downwards and are dominantly reflected in the low frequency modes.

5. Conclusions

We have reported a combined theoretical and experimental study of the lattice dynamics of tetragonal PbVO_3 and carried out a detailed comparison with the isostructural compound PbTiO_3 . All zone-center transverse optical (TO) phonon modes in PbVO_3 have been identified by a combined polarized, angle-dependent Raman spectroscopy and first-principles density functional theory simulations. The comparison between the phonon eigenvectors shows that in spite of their differences in chemistry and strain, PbVO_3 and PbTiO_3 are remarkable similar, and that the soft mode concept can be carried over to PbVO_3 by considering the evolution of its projection onto the polar (and Raman

active) modes. Differences in phonon frequencies, however, clearly reflect changes in bond strength that accompany modifications in chemical bonding. This, in particular, results in a lower value for the V-O vanadyl stretching mode as compared to other vanadium-based compounds. This work will be instrumental in studies of potential $\text{Pb}(\text{Ti},\text{V})\text{O}_3$ solid solutions and their characterization by Raman spectroscopy. Finally, we have also pointed out a strong dependence of some phonon frequencies upon magnetic order, i.e. a very strong spin-phonon coupling that will have to be investigated in future works, in relation to clarifying the magnetic ground state of PbVO_3 .

Acknowledgements

PB and JAM acknowledge the French CNRS and C. Goujon, C. Felix, S. Douillet, Ch. Bouchard and A. Prat for their technical support. PB acknowledges C. Darie, C. Colin and P. Bordet (Institut Néel) for providing us the powder synthesized at high-temperature and high-pressure from which were found the crystals used in this study and V. Dmitriev for critical reading of the manuscript. JAM acknowledges Fundação para a Ciência e Tecnologia for the Sabbatical Grant SFRH/BSAB/142869/2018. AS and EB acknowledge the FRS-FNRS for funding. AS and EB also acknowledge the CECI supercomputer facilities funded by the F.R.S-FNRS (Grant No. 2.5020.1), the Tier-1 super-computer of the Fédération Wallonie-Bruxelles funded by the Walloon Region (Grant No. 1117545) and the OFFSPRING PRACE project (DECI resource BEM supercomputer based in Poland at Wrocław).

Lattice dynamics and Raman spectrum of supertetragonal PbVO_3 .

P. Bouvier¹, A. Sasani², E. Bousquet², M. Guennou³, J. Agostinho Moreira⁴

¹ *Université Grenoble Alpes, Institut Néel CNRS, 25 Rue des Martyrs, 38042, Grenoble, France.*

² *Université de Liège, CESAM, QMAT, Physique Théorique des Matériaux, 19 Allée du 6 aout, B-4000, Sart Tilman, Belgium.*

³ *Department of Physics and Materials Science, University of Luxembourg, 41 rue du Brill, L-4422 Belvaux, Luxembourg.*

⁴ *IFIMUP – Instituto de Física de Materiais Avançados, Nanotecnologia e Fotónica, Departamento de Física e Astronomia, Faculdade de Ciências da Universidade do Porto. Rua do Campo Alegre s/n. 4169-007 Porto, Portugal.*

Figures

Figure 1. Sketch of the two reference frames chosen in this work. The laboratory reference frame (X,Y,Z) is fixed. The Y-axis is parallel to both the incident laser beam (\vec{k}_i) and the scattered signal (\vec{k}_s). The V and H polarization directions of the incident and scattered electric field are kept fixed along X and Z, respectively. The sample referential frame (x,y,z) is oriented along the tetragonal axes (a,b,c) is rotated by θ over 180° .

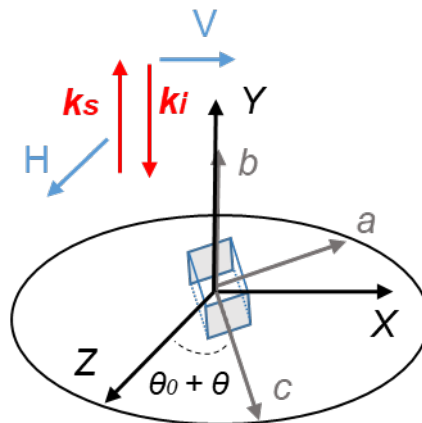


Figure 2. Representative Raman spectra of PbVO₃ recorded in the 100–1000 cm⁻¹ spectral range in the HV-scattering geometry at room conditions using the 514.5 nm and 488 nm laser lines as excitations. The wavenumber of the eight observed first-order Raman bands is reported over each band.

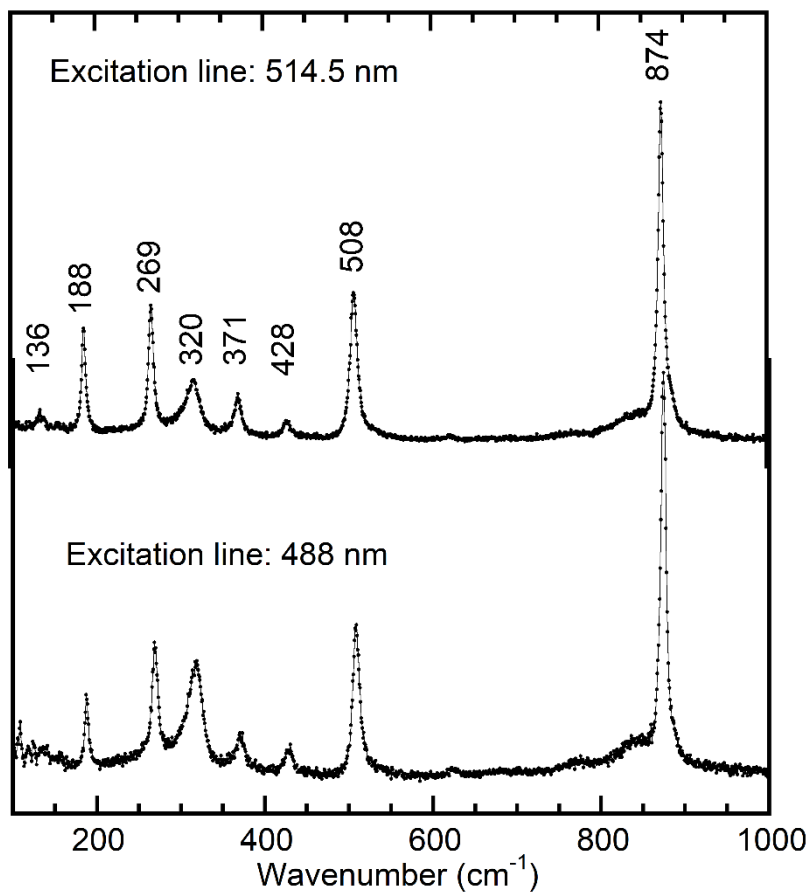


Figure 3. Raman spectra of PbVO_3 recorded, at room conditions, in the $100\text{-}1000\text{ cm}^{-1}$ spectral range using the 514.5 nm line as excitation, for the (a) VV-, (b) HV-scattering geometries at some selected azimuthal angles. The angles are indicated on the side of each spectrum.

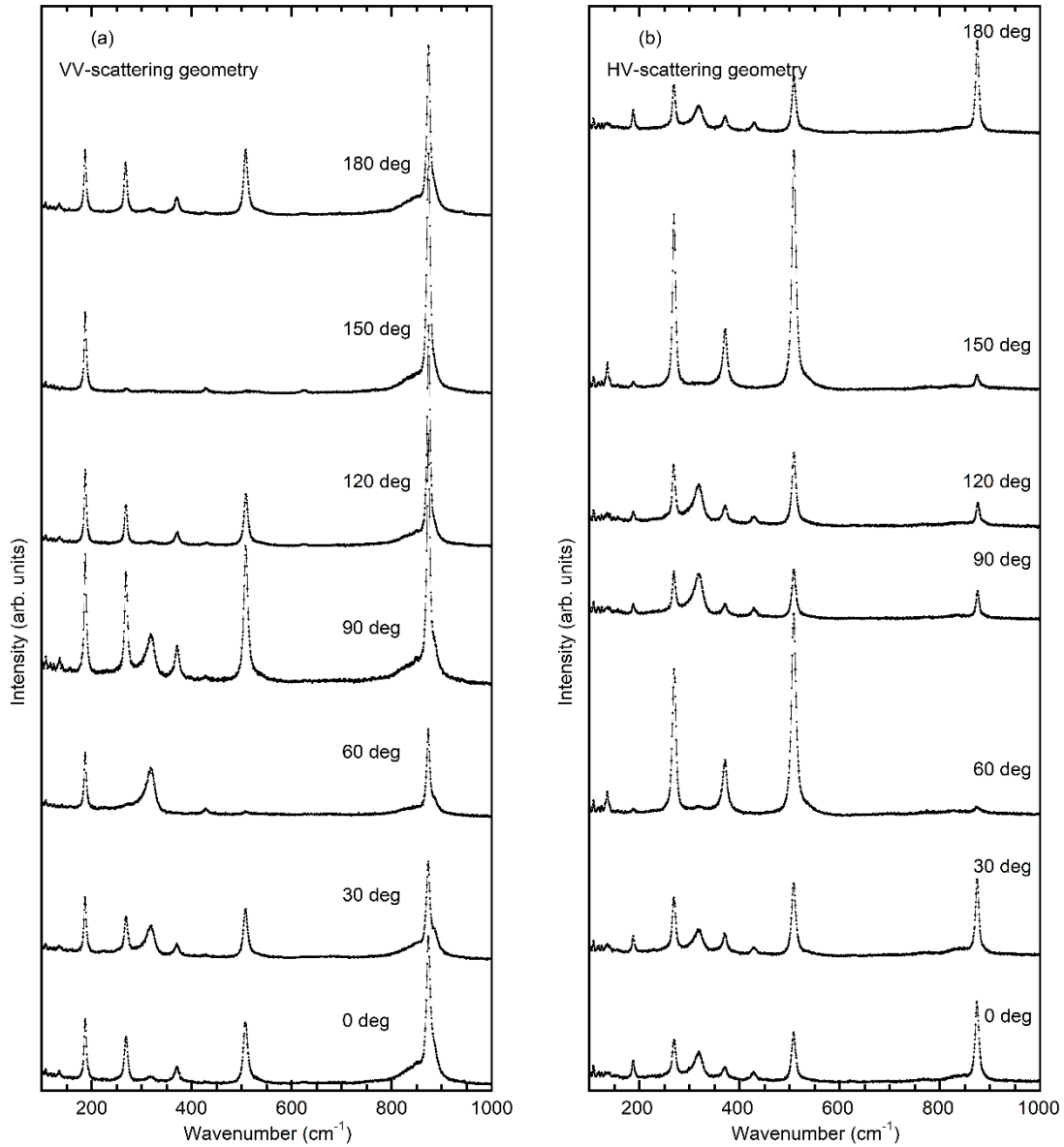


Figure 4. Polar plot of the intensity of the Raman bands centered at (a) 136, (b) 269, (c) 374, and (d) 508 cm^{-1} , measured in the VV and VH scattering geometries. The solid lines were determined through the best fit of Equations (13) and (14) to the experimental results, respectively.

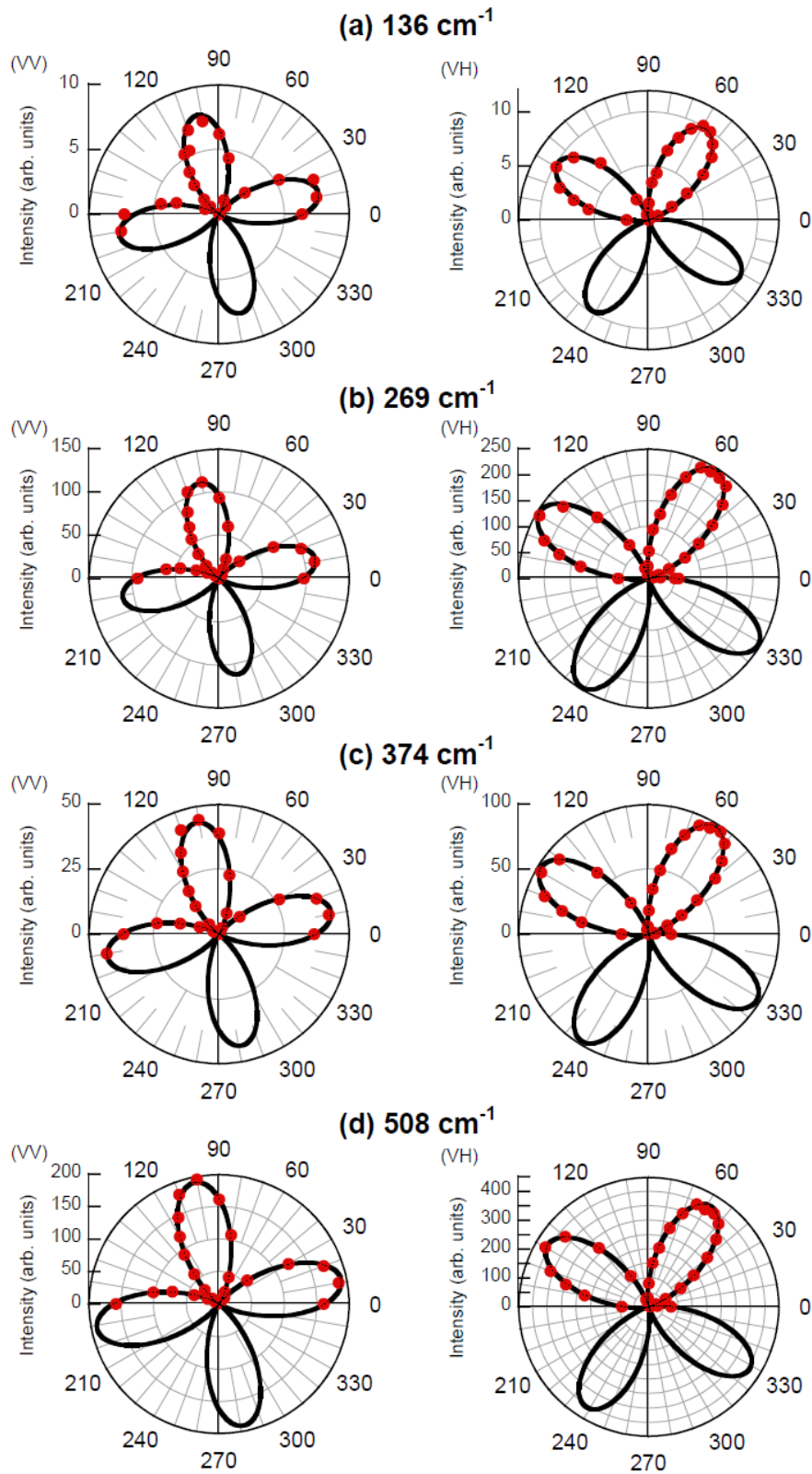


Figure 5. Polar plot of the intensity of the Raman bands centered at (a) 188, (b) 429, and (c) 874 cm^{-1} , measured in the VV and VH scattering geometries. The solid lines were determined through the best fit of Equations (7) and (8) to the experimental results, respectively.

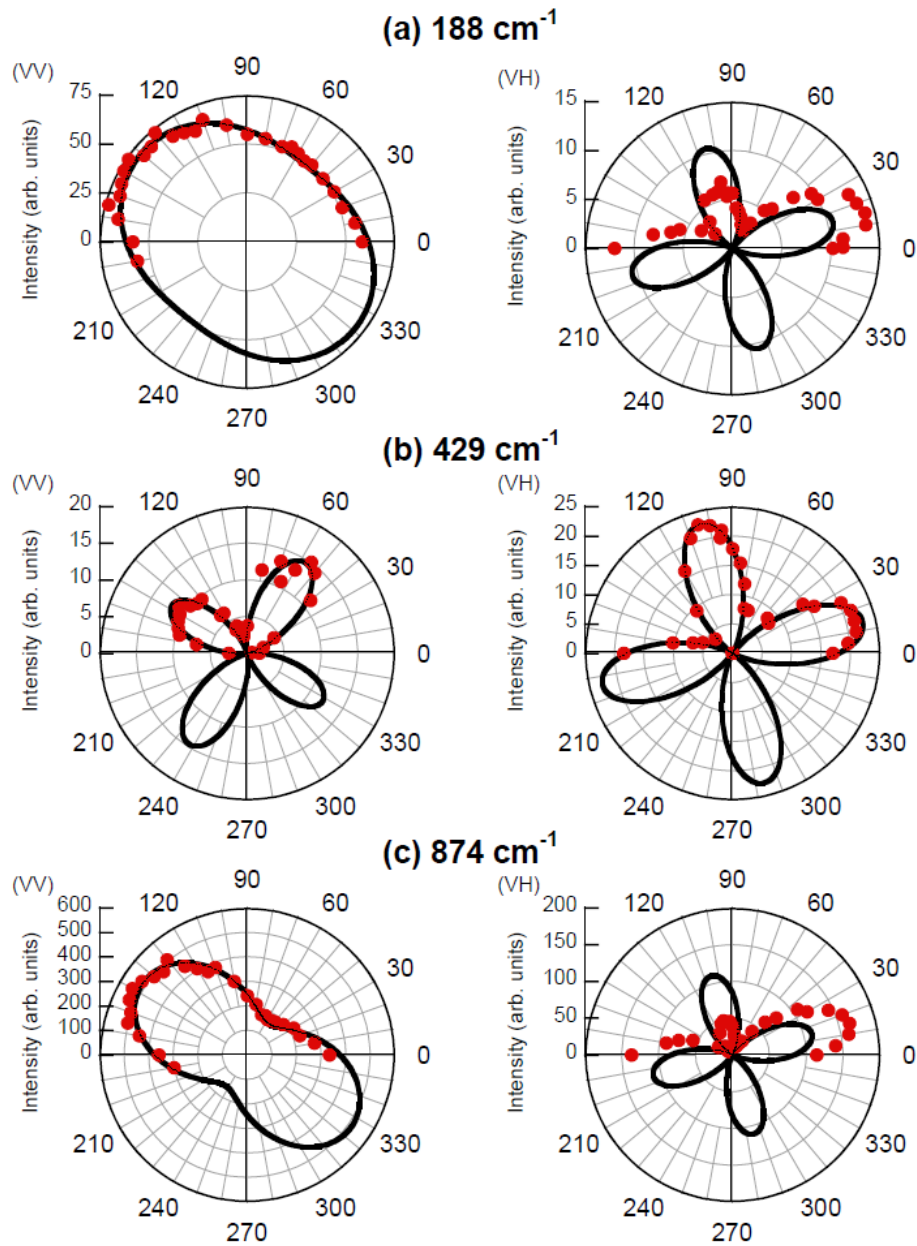


Figure 6. Representative examples of the Raman spectra of PbVO_3 in the $320 - 350 \text{ cm}^{-1}$ spectral range, recorded in VV- scattering geometry and 60° azimuthal angles. The green and blue solid lines were calculated from the best fit of an asymmetric Fano-type shape and a damped oscillator function, respectively, to the experimental results, while the black curve is their sum, along with the background.

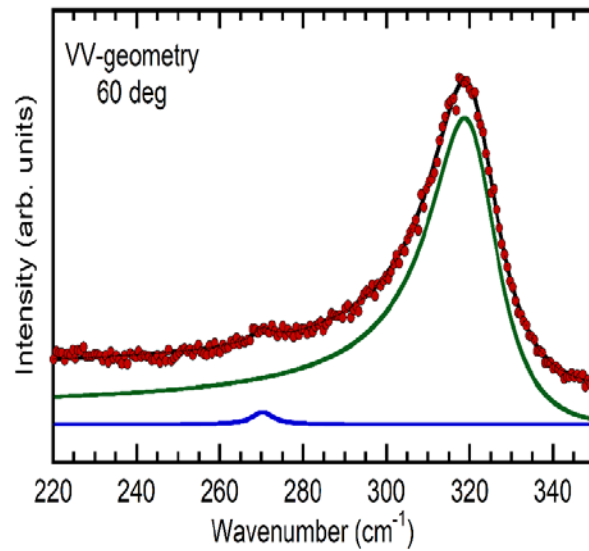


Figure 7. Polar plot of the intensity of the Raman band centered at 319 cm^{-1} , measured in the VV and VH scattering geometries. The solid lines were determined through the best fit of Equations (10) and (11) to the experimental results, respectively.

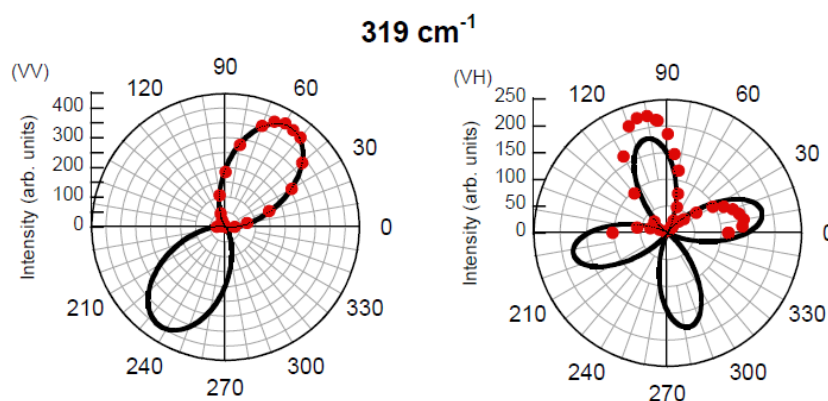


Figure 8: Schematic representation of the modes displacements and their associated wavenumbers calculated from our DFT simulations. The gray, gold and red balls corresponds to Pb, V and O atoms respectively. The arrows show the displacement of each atom and their different colors (blue vs brown) gives the sign of the atom displacements. The tetragonal *a*-, *b*- and *c*- crystallographic axes are reported on the left down side of each figure.

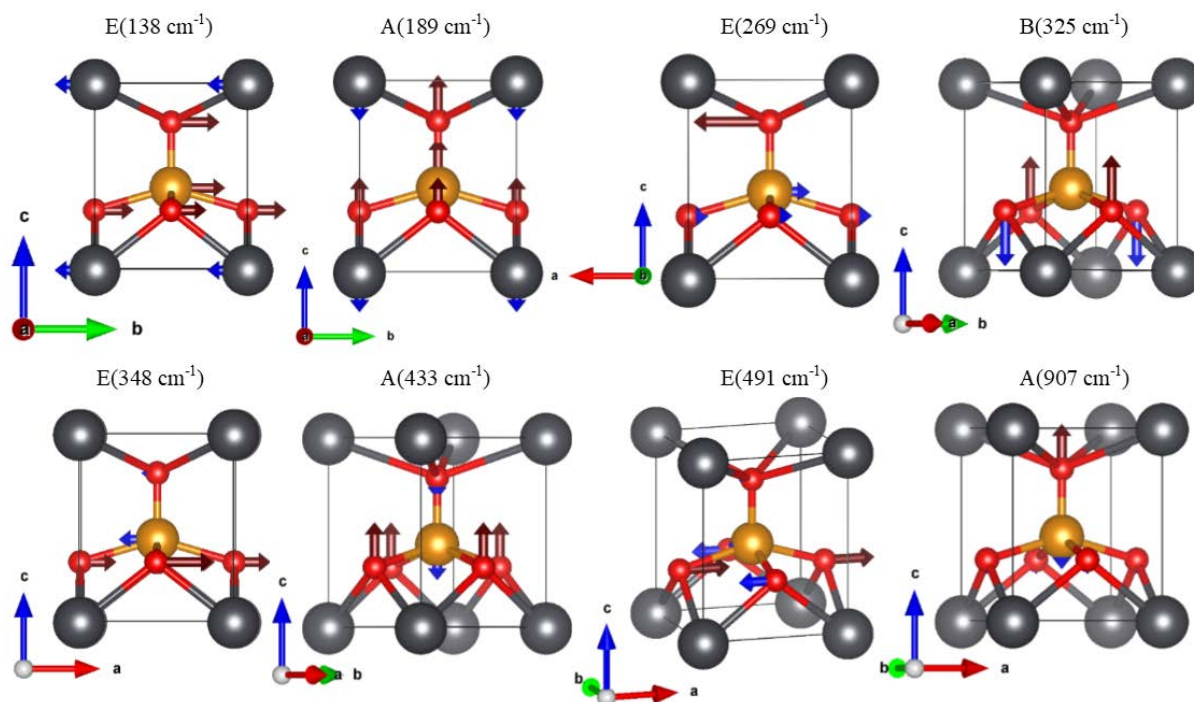
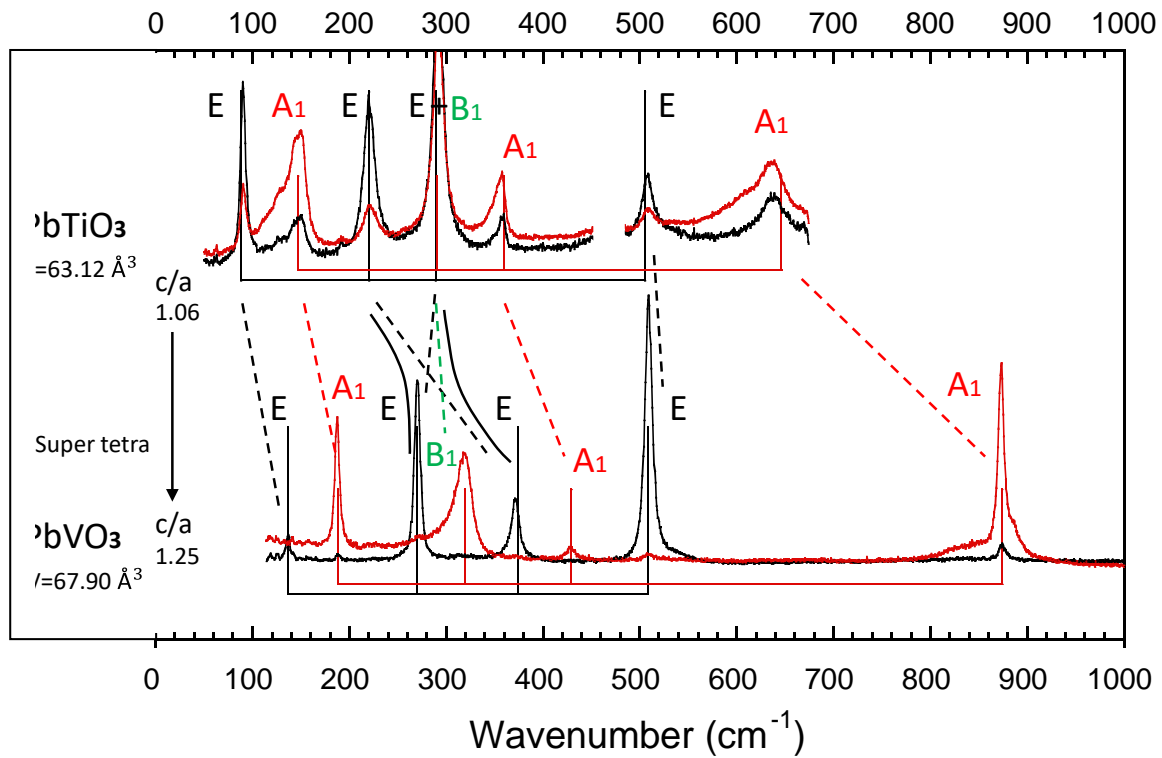


Figure 9: Sketch of the correspondence between the transversal optic Raman active phonons in PbTiO_3 and in PbVO_3 single crystals. The lines between both spectra highlight the hypothetical increase of the tetragonal ratio c/a from 1.06 to 1.25. The black and red colors correspond to two specific polarization configurations to highlight either the E or A_1 modes.



Tables

Table 1. Occupied Wyckoff positions in the primitive cell of PbVO₃ and their contribution to the Raman-active modes. The Pb atoms are placed at the origin of the unit cell as in reference [10].

Atom	Wyckoff position	A ₁	B ₁	E
Pb	1a	1		1
V/O(1)	1b	1		1
O(2)	2c	1	1	2

Table 2. Angular dependence of the intensity of the A₁, B₁ and E Raman bands in the different polarization geometries.

Symmetry	Scattering geometry	Intensity versus θ	Eq.
A ₁	VV	$I(\theta) \propto \alpha \sin^2(\theta + \theta_o) + \beta \cos^2(\theta + \theta_o) ^2$	(7)
	VH/HV	$I(\theta) \propto \left \frac{(\beta - \alpha)}{2} \sin 2(\theta + \theta_o) \right ^2$	(8)
	HH	$I(\theta) \propto \alpha \cos^2(\theta + \theta_o) + \beta \sin^2(\theta + \theta_o) ^2$	(9)
B ₁	VV	$I(\theta) \propto \gamma \sin^2(\theta + \theta_o) ^2$	(10)
	VH/HV	$I(\theta) \propto \left \frac{\gamma}{2} \sin 2(\theta + \theta_o) \right ^2$	(11)
	HH	$I(\theta) \propto \gamma \cos^2(\theta + \theta_o) ^2$	(12)
E	VV	$I(\theta) \propto \delta \sin 2(\theta + \theta_o) ^2$	(13)
	VH/HV	$I(\theta) \propto \delta \cos 2(\theta + \theta_o) ^2$	(14)
	HH	$I(\theta) \propto \delta \sin 2(\theta + \theta_o) ^2$	(15)

Table 3. Experimental values of the A₁, B₁ and E Raman tensor elements, calculated from the best fit of the angular dependence of the intensity (see Table 2) measured in PbVO₃ in three polarized VV, VH and HV- scattering configurations. Errors on the last digit are given in parenthesis.

Wavenumber (cm ⁻¹)	Symmetry	VV		VH		HV	
		α	β	α	β	α	β
188	A ₁	7.02(6)	8.39(5)	5(1)	10(2)	6(1)	9(1)
429		3.83(9)	-3.48(9)	5(1)	-5(1)	3(1)	-3(1)
874		12.50(30)	22.68(15)	5(1)	25(1)	9(1)	20(1)
319	B ₁	γ					
		19.96(7)		26.82(62)		17.72(31)	
	E	δ					
136		2.79(2)		3.14(2)		1.87(1)	
269		10.61(5)		15.66(6)		8.99(5)	
374		6.61(3)		9.86(2)		5.76(2)	
508		13.82(4)		20.22(5)		11.94(5)	

Table 4. Experimental and theoretical positions, and corresponding symmetry assignment of the first-order Raman bands of PbVO_3 in the tetragonal $P4mm$ structure.

Experimental (this study)		DFT (HSE06, this study)		DFT (LAPW, from ref. [15])
Wavenumber (cm^{-1})	Symmetry	Wavenumber (cm^{-1})	Symmetry	Wavenumber (cm^{-1})
136	E(TO)	138	E	190
188	A_1 (TO)	189	A_1	
269	E(TO) : "silent"	269	E	408
319	B_1 : "silent"	326	B_1	
374	E(TO)	349	E	
429	A_1 (TO)	434	A_1	
508	E(TO)	492	E	838
874	A_1 (TO)	907	A_1	

Table 5. Projection of the phonon eigenvectors calculated for the ground state of PbVO_3 (PVO-GS) against the phonon eigenvectors of an artificial supertetragonal PbTiO_3 calculated at a c/a ratio equal to 1.25 (PTO-ST). A perfect match gives an overlap of 1. The largest overlaps are highlighted by the color scale.

		PVO GS				PTO ST			B_1
		E(1) 138	E(2) 269	E(3) 349	E(4) 492	A_1 (1) 189	A_1 (2) 434	A_1 (3) 909	
E(1)	108	0,99	0,00	0,00	0,00				
E(2)	271	0,00	0,13	0,88	0,00				
E(3)	277	0,00	0,87	0,11	0,00				
E(4)	538	0,00	0,00	0,00	0,99				
A_1 (1)	178					0,99	0,02	0,00	
A_1 (2)	423					0,01	0,98	0,00	
A_1 (3)	771					0,00	0,00	1,00	
B_1	282							1	

Table 6: Projection of the phonon eigenvectors of the PbVO_3 and PbTiO_3 ground states (PVO GS and PTO GS respectively) against the ones of the cubic phase of PbTiO_3 . By symmetry, the B_1 mode has a perfect overlap with the cubic T_{2u} mode and is omitted here. The largest overlaps are highlighted by the color scale. The star* is to stress that the E(2) and E(3) modes of PVO have been swapped, consistent with the observation from Table 5. Wavenumber in cm^{-1} .

				$A_1(1)$	$A_1(2)$	$A_1(3)$	E(1)	E(2)	E(3)	E(4)
			PTO	152	367	678	104	213	291	515
			PVO	189	434	909	138	349*	269*	492
Modes of cubic PTO	$T_{1u}(1)$	-161	on PTO	0,29	0,53	0,18	0,36	0,62	0,00	0,01
	$T_{1u}(1)$	-161	on PVO	0,16	0,55	0,30	0,15	0,59	0,24	0,02
	$T_{1u}(2)$	117	on PTO	0,71	0,19	0,10	0,63	0,34	0,02	0,00
	$T_{1u}(2)$	117	on PVO	0,81	0,03	0,13	0,83	0,06	0,07	0,02
	T_{2u}	246	on PTO				0,00	0,03	0,93	0,03
	T_{2u}	246	on PVO				0,00	0,35	0,53	0,12
	$T_{1u}(3)$	501	on PTO	0,00	0,27	0,72	0,00	0,01	0,04	0,95
	$T_{1u}(3)$	501	on PVO	0,03	0,42	0,56	0,00	0,00	0,16	0,84

Supplemental Information

Lattice dynamics and Raman spectrum of supertetragonal PbVO_3 .

P. Bouvier¹, A. Sasani², E. Bousquet², M. Guennou³, J. Agostinho Moreira⁴

¹ *Université Grenoble Alpes, Institut Néel CNRS, 25 Rue des Martyrs, 38042, Grenoble, France.*

² *Université de Liège, CESAM, QMAT, Physique Théorique des Matériaux, 19 Allée du 6 aout, B-4000, Sart Tilman, Belgium.*

³ *Department of Physics and Materials Science, University of Luxembourg, 41 rue du Brill, L-4422 Belvaux, Luxembourg.*

⁴ *IFIMUP – Instituto de Física de Materiais Avançados, Nanotecnologia e Fotónica, Departamento de Física e Astronomia, Faculdade de Ciências da Universidade do Porto. Rua do Campo Alegre s/n. 4169-007 Porto, Portugal.*

Figure S.1. Raman spectrum of Chervetite $\text{Pb}_2\text{V}_2\text{O}_7$ recorded at room conditions.

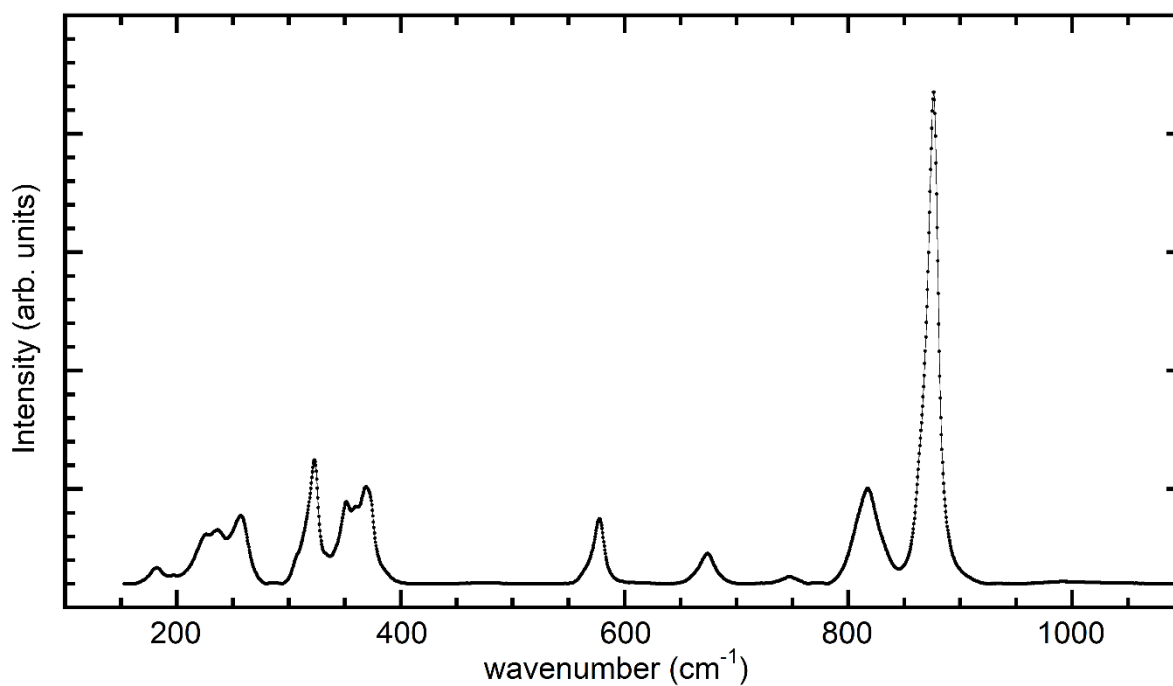


Table S.2: Eigendisplacements of the different modes in the ground state tetragonal polar $P4mm$ structure of $PbVO_3$. The values are in angstrom units.

Symmetry	E	A ₁	E	B ₁	E	A ₁	E	A ₁
Wavenumber (cm ⁻¹)	138	189	269	325	348	433	491	907
Pb	x	0	0	0.0015	0	0	0	0
	y	-0.0366	0	0	0	-0.0022	0	0
	z	0	-0.0312	0	0	0	-0.0022	0.0009
V	x	0	0	-0.0398	0	0	0	-0.0092
	y	0.0809	0	0	0	-0.0415	0	0.0000
	z	0	0.0686	0	0	0	-0.0342	0
O(1)	x	0	0	0.1486	0	0	0	-0.0059
	y	0.0913	0	0	0	-0.0104	0	0
	z	0	0.0811	0	0	0	-0.0239	0.0788
O(2)	x	0	0	-0.0232	0	0	0	-0.0674
	y	0.0676	0	0	0	0.0604	0	0
	z	0	0.053	0	-0.1075	0	0.0806	0
O(3)	x	0	0	-0.0182	0	0	0	0.1023
	y	0.0589	0	0	0	0.1107	0	0
	z	0	0.053	0	0.1075	0	0.0806	0

Figure S.3: V-O(1) stretching mode wavenumber as a function of V-O(1) bond length, for different vanadyl containing compounds. The solid line was calculated from the best fit of Badger's equation to the values concerning CaV_2O_5 , α' - NaV_2O_5 and α - V_2O_5 (see the text).

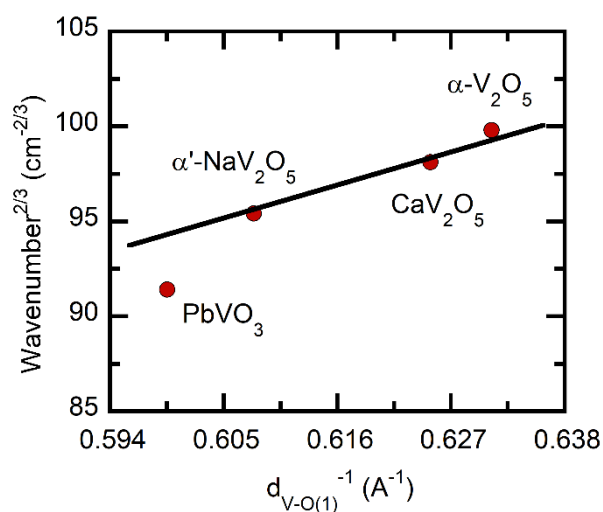


Table S.4: Atomic positions in PbVO_3 and PbTiO_3 in super tetragonal phases. Units are in angstroms

Atom	x	y	z
PbVO_3			
Pb	0.000	0.000	-0.035
V	1.902	1.902	2.020
O	1.902	1.902	-0.973
O	1.902	0.000	1.463
O	0.000	1.902	1.463
PbTiO_3			
Pb	0.000	0.000	-0.112
Ti	1.902	1.902	1.988
O	1.902	1.902	-0.903
O	1.902	0.000	1.482
O	0.000	1.902	1.482

Table S.5: Diagonal components of the Born effective charges of PbVO_3 and PbTiO_3 in super tetragonal phases. Non-diagonal components are zero. The units are in elementary charge.

atom	x	y	z
PbVO_3			
Pb	3.3191	3.3191	3.3219
V	4.4392	4.4392	4.4093
O	-1.542	-1.542	-3.8162
O	-2.2999	-3.9165	-1.9575
O	-3.9165	-2.2999	-1.9575
PbTiO_3			
Pb	3.5524	3.5524	3.3337
Ti	5.4111	5.4111	4.8621
O	-1.9265	-1.9265	-4.0447
O	-2.5286	-4.5084	-2.0755
O	-4.5084	-2.5286	-2.0755

Table S.6: Eigendisplacements of the different modes in the cubic Pm-3m structure of PbTiO₃. The values are in angstrom units.

Symmetry		T _{1u}	T _{1u}	T _{2u}	T _{1u}
Wavenumber (cm ⁻¹)		161i	117	246	501
Pb	x	-0.015	0	0	-0.001
	y	0	-0.036	0	0
	z	0	0	0	0
Ti	x	-0.048	0	0	0.0028
	y	0	0.1221	0	0
	z	0	0	0	0
O(1)	x	0.113	0	0.1236	-0.048
	y	0	0.0379	0	0
	z	0	0	0	0
O(2)	x	0.1075	0	0	0.1021
	y	0	0.0379	0	0
	z	0	0	0	0
O(3)	x	0.113	0	-0.124	-0.048
	y	0	0.0201	0	0
	z	0	0	0	0

References

- [1]- J.P. Remeika, A.M. Glass, *Mat. Res. Bull.* 5 (1970) 37-45.
- [2]- M.J. Haun, E. Furman, S.J. Jang, H.A. McKinstry, L.E. Cross, *J. Appl. Phys.* 62 (1987) 3331-3338.
- [3]- H. Béa, B. Dupé, S. Fusil, R. Mattana, E. Jacquet, B. Warot-Fonrose, F. Wilhelm, A. Rogalev, S. Petit, V. Cros, A. Anane, F. Petroff, K. Bouzouane, G. Geneste, B. Dkhil, S. Lisenkov, I. Ponomareva, L. Bellaiche, M. Bibes, A. Barthélémy, *Phys. Rev. Letters* 102 (2009) 217603.
- [4]- A.A. Belik, S. Iikubo, K. Kodama, N. Igawa, S.-I. Shamoto, S. Niitaka, M. Azuma, Y. Shimakawa, M. Takano, F. Izumi, E. Takayama-Muromachi, *Chem. Mater.* 18 (2006) 798-83.
- [5]- R. Yu, H. Hojo, K. Oka, T. Watanuki, A. Machida, K. Shimizu, K. Nakano, M. Azuma, *Chem. Mater.* 27 (2015) 2012-2017.
- [6]- M.R. Suchomel, P.K. Davies, *Appl. Phys. Letters* 86 (2005) 2662905.
- [7]- Z. Pan, X. Jiang, J. Chen, L. Hu, R. Yu, H. Yamamoto, L. Zhang, L. Fan, Y. Li, G. Li, Y. Ren, Z. Lin, M. Azuma, X. Xing, *Inorg. Chem. Front.* 5 (2018) 1277.
- [8]- M. Guennou, P. Bouvier, P. Toulemonde, C. Darie, C. Goujon, P. Bordet, M. Hanfland, J. Kreisel, *Phys. Rev. Lett.*, 112 (2014) 075501 1-5.
- [9]- R.V. Shpanchenko, V.V. Chernaya, A.A. Tsirlin, P.S. Chizhov, D.E. Sklovsky, E.V. Antipov, E.P. Hhlybov, V. Pomjakushin, A.M. Balagurov, J.E. Medvedeva, E.E. Kaul, Ch. Geibel, *Chem. Mater.* 16 (2004) 3267-3273.
- [10]- A.A. Belik, M. Azuma, T. Saito, Y. Shimakawa, M. Takano, *Chem. Mater.* 17 (2005) 269-273.
- [11]- A.A. Belik, T. Yamauchi, H. Ueda, Y. Ueda, H. Yusa, N. Hirao, M. Azuma, *J. of the Physical Society of Japan* 83 (2014) 074711.
- [12]- Y. Uratani, T. Shishidou, F. Ishii, T. Oguchi, *Jpn. J. Appl. Phys.*, 44 (2005), 7130-7133.
- [13]- A. Kumar, L.W. Martin, S. Denev, J.B. Kortright, Y. Suzuki, R. Ramesh, V. Gopalan, *Phys. Rev. B* 75 (2007) 060101R.

-
- [14]- Y. Yamada, V. Garcia, S. Fusil, S. Boyn, M. Marinova, A. Gloter, S. Xavier, J. Grollier, E. Jacquet, C. Carretero, C. Deranlot, M. Bibes, A. Barthelemy, *ACS Nano*, 7 (2013) 5385-5390.
- [15]- D.J. Singh, *Phys. Rev. B*, 73 (2006) 094102.
- [16]- K. Oka, I. Yamada, M. Azuma, S. Takeshita, K.H. Satoh, A. Koda, R. Kadono, M. Takano, Y. Shimakawa, *Inorg. Chem.*, 47 (2008) 7355-7359.
- [17]- A.A. Tsirlin, A.A. Belik, R.V. Shpanchenko, E.V. Antipov, E. Takayama-Muromacji, H. Rosner, *Phys. Rev. B*, 77 (2008) 092402.
- [18]- K. Oka, T. Yamauchi, S. Kanungo, T. Shimazu, K. Oh-ishi, Y. Uwatoko, M. Azuma, T. Saha-Dasgupta, *J. Phys. Soc. Japan* 87 (2018) 024801.
- [19]- X. Ming, J.-W. Yin, X.-L. Wang, C.-Z. Wang, Z.-F. Huang, G. Chen, *Solid State Sciences*, 12 (2010) 938-945.
- [20]- A. Okos, C. Colin, C. Darie, O. Raita, P. Bordet, A. Pop, *J Alloys and Compounds* 602 (2014) 265-268.
- [21]- L. W. Martin, Q. Zhan, Y. Suzuki, R. Ramesh, M. Chi, N. Browning, T. Mizoguchi, J. Kreisel, *Appl. Phys. Lett.* 90 (2007) 062903.
- [22]- S.H. Oh, H.-J. Jin, H.-Y. Shin, R.H. Shin, S. Yoon, Y.-S. Seo, J.-S. Ahn, W. Jo, *J. Phys. D: Appl. Phys.* 47 (2014) 245302.
- [23]- R. Dovesi, A. Erba, R. Orlando, C. M. Zicovich-Wilson, B. Civalleri, L. Maschio, M. Rerat, S. Casassa, J. Baima, S. Salustro, B. Kirtman, 4, (2018) *WIREs Comput Mol Sci*, Vol. 8, p. e1369.
- [24]- A.V. Krukau, O.A. Vydrov, A.F. Izmaylov, G.E. Scuseria, 22, (2006) *The Journal of Chemical Physics*, Vol. 125, p. 224106.
- [25]- J.P. Perdew, K. Burke, M. Ernzerhof, 18 (1996) *Phys. Rev. Lett.*, Vol. 77, pp. 3865-3868.
- [26]- F. Pascale, C.M. Zicovich-Wilson, F. Lopez, B. Civalleri, R. Orlando, R. Dovesi. 6, (2004), *Journal of computational chemistry*, Vol. 25, pp. 888-897.
- [27]- C.M. Zicovich-Wilson, F. Pascale, C. Roetti, V.R. Saunders, R. Orlando, R. Dovesi. 15, (2004) *Journal of Computational Chemistry*, Vol. 25, pp. 1873-1881.
- [28]- G. Sophia, Ph. Baranek, Ch. Sarrazin, M. Rérat, R. Dovesi. 11, s.l. : Taylor & Francis, (2013), *Phase Transitions*, Vol. 86, pp. 1069-1084.
- [29]- D. Vilela Oliveira, J. Laun, M.F. Peintinger, T. Bredow, 27, (2019), *Journal of Computational Chemistry*, Vol. 40, pp. 2364-2376.
- [30]- F. Corà, 18, s.l. : Taylor & Francis, 2483-2496, *Molecular Physics*, Vol. 103, p. 2005.
- [31]- H.T. Stokes, D.M. Hatch, 1, 2 (2005) , *Journal of Applied Crystallography*, Vol. 38, pp. 237-238.
- [32]- G. Burns, B.A. Scott, *Phys. Rev. B*, 7 (1973) 3088-3101.
- [33]- R.A. Frey, E. Silberman, *Helvetica Physica Acta*, 49 (1976) 1-11.
- [34]- R.H. Lyddane, R.G. Sachs, E. Teller, *Phys. Rev.*, 59 (1941) 673-676.
- [35]- L. Merten, *Z. Naturforsch*, 15a, 47 (1962).
- [36]- U. Fano., *Phys. Rev.*, 124 (1961) 1866.
- [37]- R. M. Badger, *J. Chem. Phys.* 2 (1934) 128-131.
- [38]- Z.V. Popovic, *J. Phys. Cond. Matter* 14 (2002) L583-L589.
- [39]- I. Loa, K. Syassen, R.K. Kremer, *Solid State Communications* 112 (1999) 681-685.
- [40]- A. Grzechnik, *Chem Mater* 10 (1998) 2505-2509.
- [41]- C. Sanchez, J. Livage, G. Lucazeau, *J. Raman spectroscopy* 12 (1982) 68-72.
- [42]- L. Abello, E. Husson, Y. Repelin, G. Lucazeau, *Spectrochimica Acta* 39A (1983) 641-651.
- [43]- D.L. Rousseau, S.P.S Porto, *Phys. Rev. Letters*, 20 (1968) 1354-1357.
- [44]- C.M. Foster, Z. Li, M. Grimsditch, S.-K. Chan, D.J. Lam, *Phys. Rev. B* 48 (1993) 160-167 and C.M. Foster, M. Grimsditch, Z. Li, V.G. Karpov, *Phys. Rev. Letters*, 71 (1993) 1258-1260.
- [45]- P.-E. Janolin, P. Bouvier, J. Kreisel, P.A. Thomas, I.A. Kornev, L. Bellaiche, W. Crichton, M. Hanfland, B. Dkhil, *Phys. Rev. Letters* 101 (2008) 237601.
- [46]- W.G. Nilson and J.G. Skinner, *the Journal of chemical physics*, 48 (1968) 2240-2248.
- [47]- M. El Marssi, F. Le Marrec, I. A. Lukyanchuk, and M. G. Karkut, *J. Appl. Phys.* 94, 3307 (2003).
- [48]- U.Koroglu, S.Cabuk, E.Deligoz, *Solid State Sciences* 34 (2014) 1-7.
- [49]- Z. Pan, J. Chen, X. Jiang, L. Hu, R. Yu, H. Yamamoto, T. Ogata, Y. Hattori, F. Guo, X. Fan, Y. Li, G. Li, H. Gu, Y. Ren, Z. Lin, M. Azuma, X. Xing, *J. Am. Chem. Soc.* 139 (2017) 14865-14868.
- [50]- A. Garcia, D. Vanderbilt, *Phys. Rev. B* 54 (1996) 3817-3824.
- [51]- Ph. Ghosez, E. Cockayne, U.V. Waghmare, K.M. Rabe, *Phys. Rev. B* 60 (1999) 836-843.
- [52]- S. Tinte, K.M. Rabe, D. Vanderbilt, *Phys. Rev. B* 68 (2003) 144105 1-9.
- [53]- D.I. Bilc, R. Orlando, R. Shaltaf, G.-M. Rignanese, J. Iniguez, Ph. Ghosez, *Phys. Rev. B*, 77 (2008), 165107.
- [54]- P. Hermet, M. Veithen, Ph. Ghosez, *J. Phys.: Condens. Matter* 21 (2009) 215901 1-10.